

Co_{0.6}Fe_{0.4}O-Co_{1.4}Fe_{1.6}O₄ Core-Shell Nanoparticles with Colossal Exchange Bias

Samyog Adhikari,^{a,c} Roger D. Johnson,^b Pascal Manuel,^d Leonardo Lari,^e Le Duc Tung,^{a,c} Vlado K. Lazarov^e and Nguyen Thi Kim Thanh^{*a,c}

^a Biophysics Group, Department of Physics and Astronomy, University College London, Gower Street, London, WC1E 6BT, United Kingdom. Email: ntk.thanh@ucl.ac.uk

^b Condensed Matter and Materials Physics, Department of Physics and Astronomy, University College London, Gower Street, London, WC1E 6BT, United Kingdom.

^c UCL Healthcare Biomagnetics Laboratory, The Royal Institution, 21 Albemarle Street, London, W1S 4BS, United Kingdom.

^d ISIS Neutron and Muon Source, STFC Rutherford Appleton Laboratory, Chilton, Oxfordshire, OX11 0QX, United Kingdom.

^e School of Physics, Engineering and Technology, University of York, Heslington, York, YO10 5DD, United Kingdom.

Contents

1. Transmission electron microscope (TEM) and Dynamic Light Scattering (DLS)	2
2. X-ray Diffraction (XRD)	2
3. Neutron Diffraction.....	3
4. Magnetization normalization and magnetic hysteresis loops	3
5. Thermogravimetric Analysis (TGA)	4
6. Bulk elemental composition determined by ICP-OES and EDX	6
7. X-ray Photoelectron Spectroscopy (XPS)	6
8. Multiphase Rietveld refinement results	7
9. Fourier Transform Infrared Spectroscopy (FTIR)	9
10. Ultraviolet-Visible Spectroscopy (UV-Vis)	9
11. References.....	10

The samples used in this work are labelled as follows: **CO** = pure cobalt monoxide, **CFO** = pure cobalt ferrite, **CS** = core-shell (AFM core-Co_{0.6}Fe_{0.4}O + FiM shell-Co_{1.4}Fe_{1.6}O₄).

Here, AFM = antiferromagnet and FiM = ferrimagnet.

1. Transmission electron microscope (TEM) and Dynamic Light Scattering (DLS)

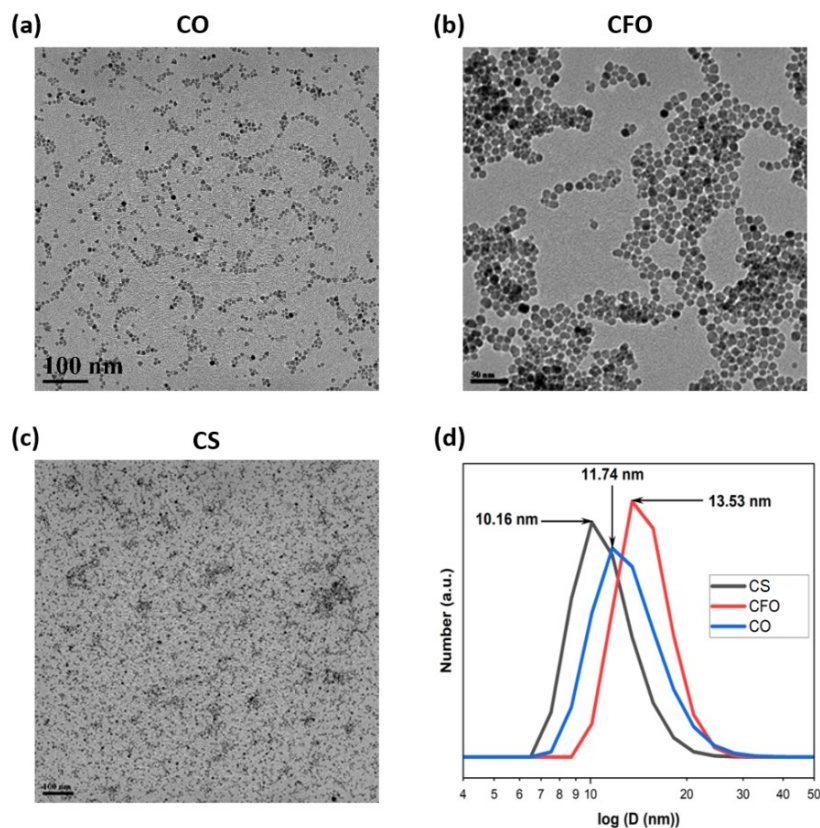


Figure S1. Low-magnification TEM images of a) pure CO, b) pure CFO, and c) biphasic CS nanoparticles. d) Solvodynamic size distribution obtained using DLS.

2. X-ray Diffraction (XRD)

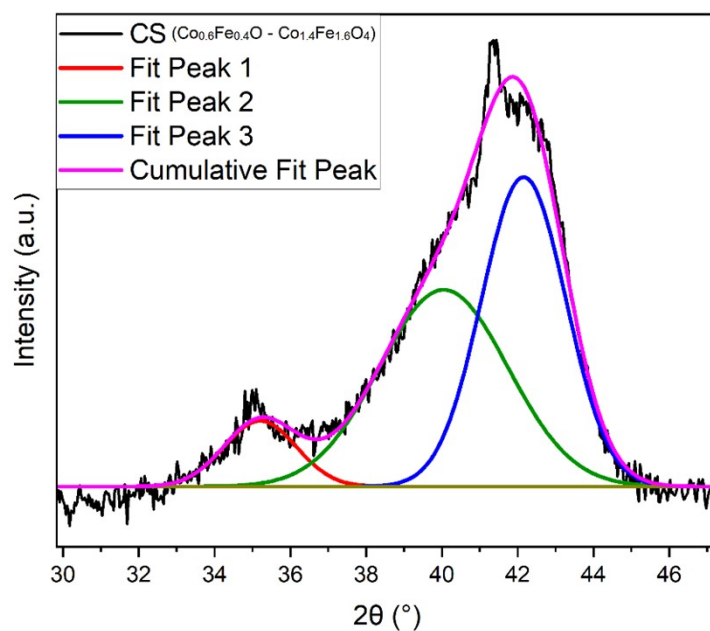


Figure S2. Deconvoluted peaks of the CS sample. Fit peak 3 is assigned to CO (111), fit peak 2 to CFO (311) peak, and fit peak 1 to CFO (220).

Equation S1. Phase fraction (PF).

$$PF = \frac{I_A}{I_A + I_B} \times 100\%$$

Where, I_A and I_B are intensity counts of face-centered cubic (Fm-3m) and hexagonal close-packed (P63mc), respectively.

3. Neutron Diffraction

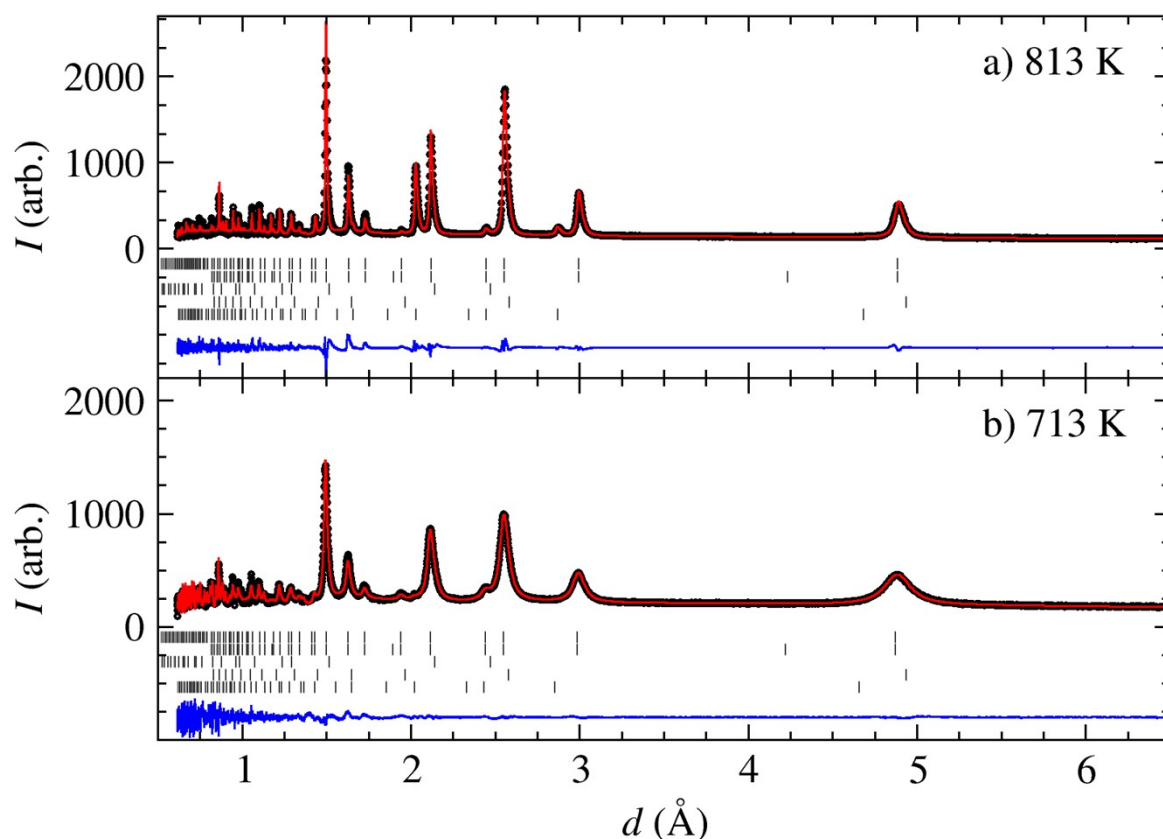


Figure S3. Representative Rietveld refinements of neutron powder diffraction data measured at a) 813 K and b) 713 K for biphasic CS nanoparticles. The observed pattern is represented by black points, and the calculated pattern is represented by the red line. The difference between the observed and calculated pattern is represented by the blue line. The black vertical tick marks indicate the positions of the nuclear CFO (top/first), magnetic CFO (second), nuclear CO (third), and magnetic CO (fourth) diffraction peaks. The bottom/fifth vertical tick mark is a spinel phase (where the CFO evolves towards the iron-rich Fe_3O_4 phase).

4. Magnetization normalization and magnetic hysteresis loops

The magnetization values presented in this paper are obtained from the SQUID-VSM instrument and given in emu g_M^{-1} , where M = iron, cobalt. The magnetization values are initially normalized for the weight fraction of the ligands using TGA data, and further normalization is performed for the weight fraction of total metal ions in the sample using ICP-OES data (Table S2).

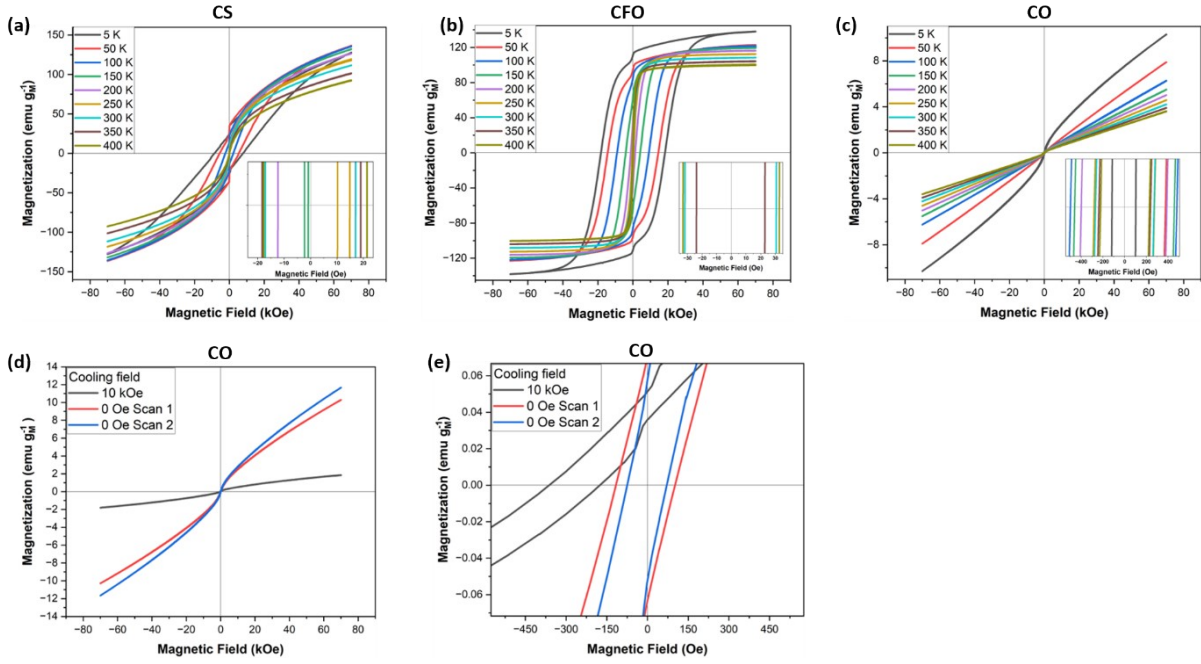


Figure S4. a) Magnetic hysteresis loops of a) biphasic CS, b) pure CFO and d) pure CO nanoparticles at different temperatures. d) Magnetic hysteresis loop of pure CO nanoparticles at 5 K under 10 kOe cooling field and repeat magnetic hysteresis loop at 5 K under no cooling field to show the random nature of disordered surface spins. e) An enlarged image shows a small exchange bias in pure CO due to interactions between disordered surfaces and ordered core spins.

Equation S2. Effective magnetic anisotropy (K_{eff}).

$$K_{eff} = \frac{25 k_B T_b}{V}$$

Where k_B is the Boltzmann constant ($1.38 \times 10^{-23} \text{ J K}^{-1}$), T_b is the blocking temperature, and V is the volume of the nanoparticles. Here, $\ln(\tau_m/\tau_0)$ is 25, a typical value for a conventional magnetometer. τ_m is the measurement time, while τ_0 is the attempt time, i.e., a fundamental timescale between successive attempts to flip the magnetization due to thermal energy.

Table S1. K_{eff} values for all samples. AFM-FiM core-shell (CS) nanoparticles exhibit two T_b peaks. A primary peak at 169 K and another peak at 316 K.

Sample	Diameter (nm)	Volume (m^3) $\times 10^{-25}$	T_b (K)	$K_{eff} (\text{J m}^{-3}) \times 10^4$
CO	8.64	3.38	7	0.71
CFO	9.79	4.91	238	16.72
CS	8.55	3.27	169* 316#	17.83* 33.33#

* The primary peak at 169 K is associated with the T_b of the biphasic CS system.

The secondary peak at 316 K likely corresponds to the T_b of the single-phase FiM spinel nanoparticles.

5. Thermogravimetric Analysis (TGA)

TGA is conducted on all samples to quantify the weight percentage of stabilizing ligands and estimate the Curie temperature. The analysis is performed by heating the sample twice from room temperature

to 973 K with a constant heating rate of $283.15 \text{ K min}^{-1}$ ($10 \text{ }^\circ\text{C min}^{-1}$) under an air atmosphere. The first heating determines the amount of ligand content, which is gradually burned off from the nanoparticle surface as the temperature increases. Initially, water is desorbed from the surface, followed by ligand evaporation and decomposition, which occur between 473–600 K, as indicated in the safety data sheet of oleylamine (OLA) and oleic acid (OA). The ligand content in the samples ranges from 8.8% to 12.6% of the total powder weight (Figure S5a, c and e, Supporting Information), with slight variations attributed to nanoparticle size, surface area, and aggregation state differences. After ligand removal, the samples were cooled to room temperature, and a second heating was conducted in a magnetic field. Above the Curie temperature, the material transitions from being magnetically attracted to the external field to being unaffected, reflected as an apparent weight loss in the TGA curve. The derivative weight loss data are used to estimate the Curie temperatures of pure CFO and biphasic CS at 759 K and 770 K, respectively, in close agreement with neutron diffraction data (Figure 2d,e). The T_N of pure CO nanoparticles could not be estimated using TGA due to its low magnetization.

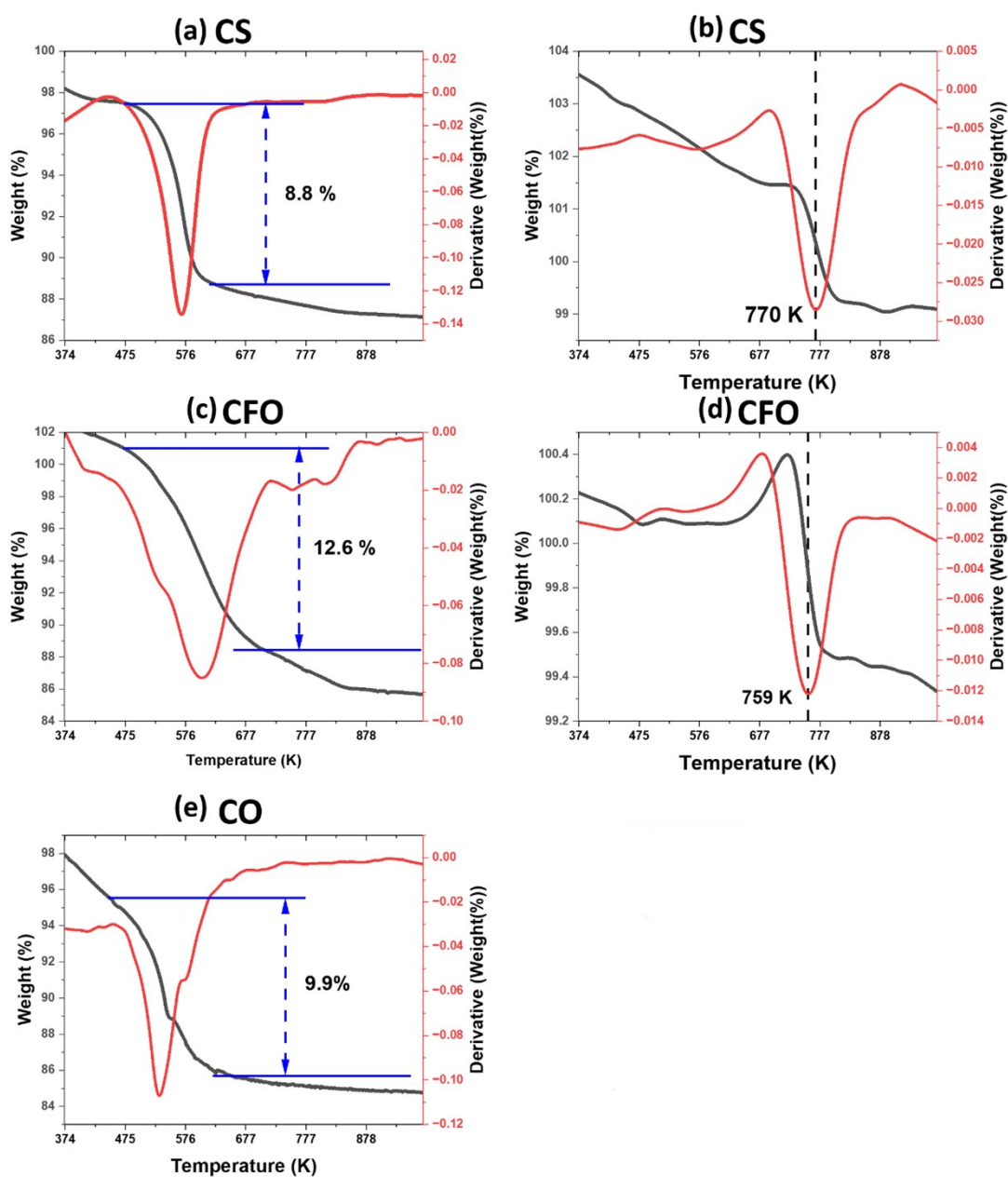


Figure S5. TGA spectra to estimate ligand content in **a)** CS, **c)** CFO, and **e)** CO nanoparticles. A second TGA scan to estimate the Curie temperature of **b)** CS and **d)** CFO nanoparticles.

6. Bulk elemental composition determined by ICP-OES and EDX

ICP-OES analysis of the CS sample revealed a bulk composition of 17.8% Co and 45.8 % Fe, indicating an excess of Fe compared to the cation stoichiometry derived from neutron diffraction data. The weight percentages of Fe and Co from EDX (39.3 % Fe and 17.1% Co) align more closely with ICP-OES. This apparent discrepancy arises from the distinct probing mechanisms of each technique. ICP-OES dissolves the entire sample to provide elemental composition. However, EDX provides local elemental composition, which may possibly underestimate the Fe-rich phases. On the other hand, neutron diffraction selectively probes the ordered arrangement of cations. Thus, the higher Fe content observed on ICP-OES and EDX may reflect contributions from disordered phases undetected by neutron diffraction.

Table S2. ICP-OES elemental composition of the bulk powder sample for pure CO, CFO and biphasic CS sample.

Sample	Concentration (ppm)		Molar concentration $\times 10^{-7}$ (mol ml ⁻¹)		Mass fraction (%)	
	Co	Fe	Co	Fe	Co	Fe
CO	66.3	N.A.	11.2	N.A.	68.8	N.A.
CFO	11.5	57.6	1.95	10.32	11.2	56.2
CS	10.9	28.0	1.85	5.02	17.8	45.8

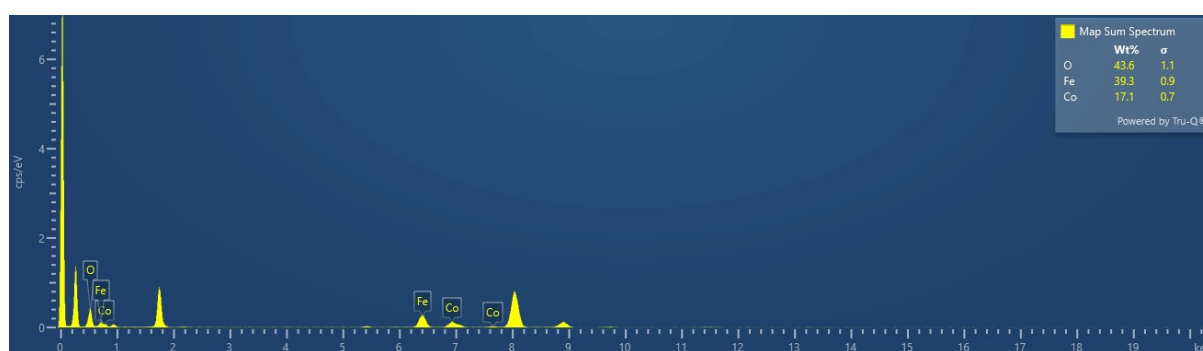


Figure S6. EDX spectra of the CS sample indicate an Fe excess.

7. X-ray Photoelectron Spectroscopy (XPS)

XPS, a surface-sensitive technique, was used to further probe the elemental composition and oxidation state of the surface layer. The Fe_{2p} spectrum exhibits binding energy peaks characteristic of Fe³⁺ species, and closely matches with the Fe₂O₃¹ or Fe(OH)₃² reference, which we attribute to the disordered phase invisible to the diffraction experiments. This finding suggests crystalline AFM-FiM core-shell nanoparticles with a Fe-rich surface layer, which corroborates the heterogeneity inferred from ICP-OES and EDX. The Co_{2p} spectrum obtained is not meaningful due to overlap with the Auger Fe peak.

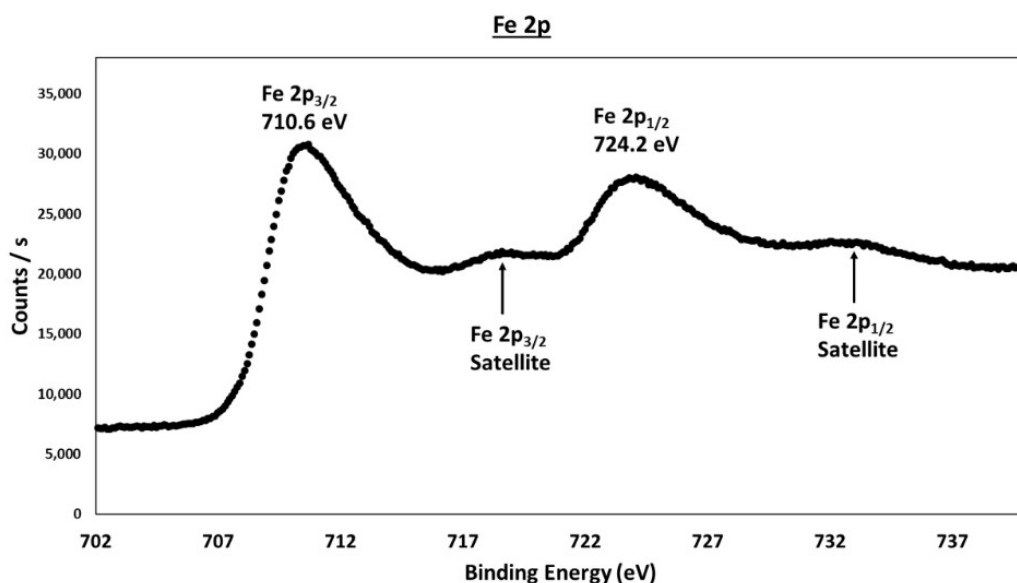


Figure S7. Fe_{2p} XPS spectra of the core-shell (CS) sample.

8. Multiphase Rietveld refinement results

The cation stoichiometry in the AFM and FiM phases was determined at the base temperature, holding the oxygen stoichiometry constant at the nominal composition. The occupancies were fixed for higher temperatures to values consistent with the chemical formulae Co_{0.6}Fe_{0.4}O-Co_{1.4}Fe_{1.6}O₄.

Table S3. Wyckoff positions and the occupancy values.

Phase	Atom	Occupancy	Wyckoff positions
FiM (Co _{1.4} Fe _{1.6} O ₄)	Co1	0.6	8a
	Fe1	0.4	8a
	Co2	0.38	16d
	Fe2	0.62	16d
	O1	1.0	32e
AFM (Co _{0.6} Fe _{0.4} O)	Co1	0.6	4a
	Fe1	0.1	4a
	O1	1.0	4b

Table S4. Crystal structure parameters of CS sample at 10K, 300K and 453 K. Excellent reliability parameters of R = 1.71 % and wR = 0.666% were achieved for the refinement of data obtained at 10K, the R = 1.68 % and wR = 0.689% were achieved for 300 K data, and the R = 1.87 % and wR = 0.811% were achieved for 453 K data.

Temperature (K)	FiM phase (Co _{1.4} Fe _{1.6} O ₄)							
	Atom	x	y	z	B (Å ²)	R-factor (%)		Cell parameter (Å)
						Bragg	Magnetic	
10	Co1	0.12500(0)	0.12500(0)	0.12500(0)	1.249(62)	3.16	1.10	8.37179(34)
	Fe1	0.12500(0)	0.12500(0)	0.12500(0)	1.249(62)			

	Co2	0.50000(0)	0.50000(0)	0.50000(0)	1.249(62)			
	Fe2	0.50000(0)	0.50000(0)	0.50000(0)	1.249(62)			
	O1	0.25253(40)	0.25253(40)	0.25253(40)	1.249(62)			
	AFM phase (Co_{0.6}Fe_{0.4}O)							
	Atom	x	y	z	B (Å²)	R-factor (%)		Cell parameter (Å)
						Bragg	Magnetic	
	Co1	0.00000(0)	0.00000(0)	0.00000(0)	0.500(0)	3.84	0.4	4.22296(45)
	Fe1	0.00000(0)	0.00000(0)	0.00000(0)	0.500(0)			
	O1	0.50000(0)	0.50000(0)	0.50000(0)	0.500(0)			
300	FiM phase (Co_{1.4}Fe_{1.6}O₄)							
	Atom	x	y	z	B (Å²)	R-factor (%)		Cell parameter (Å)
						Bragg	Magnetic	
	Co1	0.12500(0)	0.12500(0)	0.12500(0)	1.343(65)	4.02	1.35	8.38044(36)
	Fe1	0.12500(0)	0.12500(0)	0.12500(0)	1.343(65)			
	Co2	0.50000(0)	0.50000(0)	0.50000(0)	1.343(65)			
	Fe2	0.50000(0)	0.50000(0)	0.50000(0)	1.343(65)			
	O1	0.25093(44)	0.25093(44)	0.25093(44)	1.343(65)			
	O1	0.25093(44)	0.25093(44)	0.25093(44)	1.343(65)			
	AFM phase (Co_{0.6}Fe_{0.4}O)							
	Atom	x	y	z	B (Å²)	R-factor (%)		Cell parameter (Å)
						Bragg	Magnetic	
	Co1	0.00000(0)	0.00000(0)	0.00000(0)	0.500(0)	3.42	1.08	4.22876(45)
	Fe1	0.00000(0)	0.00000(0)	0.00000(0)	0.500(0)			
	O1	0.50000(0)	0.50000(0)	0.50000(0)	0.500(0)			
453	FiM phase (Co_{1.4}Fe_{1.6}O₄)							
	Atom	x	y	Z	B (Å²)	R-factor (%)		Cell parameter (Å)
						Bragg	Magnetic	
	Co1	0.12500(0)	0.12500(0)	0.12500(0)	1.729(56)	3.20	1.41	8.39954(29)
	Fe1	0.12500(0)	0.12500(0)	0.12500(0)	1.729(56)			
	Co2	0.50000(0)	0.50000(0)	0.50000(0)	1.729(56)			
	Fe2	0.50000(0)	0.50000(0)	0.50000(0)	1.729(56)			
	O1	0.25230(33)	0.25230(33)	0.25230(33)	1.729(56)			
	O1	0.25230(33)	0.25230(33)	0.25230(33)	1.729(56)			
	AFM phase (Co_{0.6}Fe_{0.4}O)							
	Atom	x	y	z	B (Å²)	R-factor (%)		Cell parameter (Å)
						Bragg	Magnetic	
	Co1	0.00000(0)	0.00000(0)	0.00000(0)	0.500(0)	3.17	N.A.	4.23763(62)
	Fe1	0.00000(0)	0.00000(0)	0.00000(0)	0.500(0)			
	O1	0.50000(0)	0.50000(0)	0.50000(0)	0.500(0)			

9. Fourier Transform Infrared Spectroscopy (FTIR)

The Fourier transform infrared (FTIR) spectra of all samples confirm the presence of stabilizing agents on the surface of nanoparticles, namely OA and OLA, as shown in Figure S8. Key characteristic bands are observed at 2925 cm^{-1} and 2854 cm^{-1} , corresponding to the asymmetric and symmetric stretching modes of CH_2 , respectively.³⁻⁶ The OA spectrum exhibits a peak at 1710 cm^{-1} , attributed to the $\text{C}=\text{O}$ stretching vibration of the carboxylic acid group, which is absent or significantly suppressed in the spectra of the ligand mixture (OA+OLA) and the synthesized nanoparticles. Notably, the spectrum of the ligand mixture is not merely a combination of the OA and OLA spectra, as new peaks appear around 1552 cm^{-1} and 1401 cm^{-1} , linked to the asymmetric and symmetric stretching of the COO^- group.³⁻⁸ All spectra also feature a peak at 1466 cm^{-1} , indicative of the in-plane O-H band in OA.³⁻⁶ Additionally, the OLA and nanoparticles exhibit a weak peak at 1064 cm^{-1} , associated with the stretching of the C-N group.⁸ The out-of-plane O-H stretch, observed in the OA spectrum at 934 cm^{-1} , is absent in the other samples.³⁻⁶

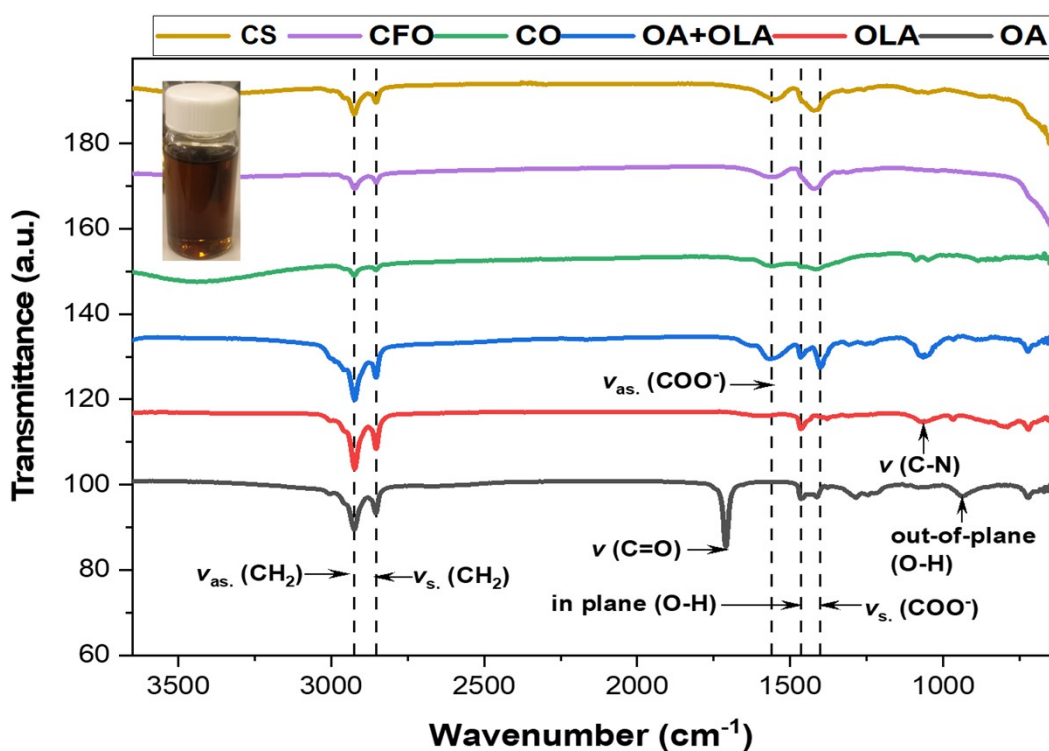


Figure S8. FTIR spectra of the initial, as synthesized powders, OA, OLA, and OA+OLA (inset shows CS nanoparticles stabilized in n-hexane due to the presence of OLA).

10. Ultraviolet-Visible Spectroscopy (UV-Vis)

Several studies have demonstrated the interplay between magnetic and optical properties in materials.⁹⁻¹¹ Materials with AFM ordering typically exhibit lower band gap energies than FM/FiM ordering due to significant differences in their electronic structures.^[65] Additionally, other material characteristics, such as morphology and doping concentration, can influence the optical band gap energies.¹³ The optical properties of all samples are investigated using ultraviolet-visible (UV-VIS) spectroscopy, and the optical band gap energy is estimated using the Tauc method.¹⁴ All samples exhibit a single peak in the UV region (250-280 nm), except for the pure CO nanoparticles, which also

show a minor broad peak around 660 nm in the visible region (Figure S8a). The UV peak at 250-280 nm observed in all samples is attributed to ligand-to-metal charge transfer, where electron movement occurs from the oxygen 2p states in the valence band to the cobalt 3d states in the conduction band.¹⁵ In the case of pure CO, the visible peak around 650 nm is linked to metal-to-metal charge transfer involving Co^{2+} and Co^{3+} states, possibly indicating the presence of trace Co_3O_4 .¹⁶ This phase might either arise during synthesis or from oxidation upon exposure to laser irradiation.^{17,18} All samples' direct transition band gap values are similar, ranging from 3.8 to 3.9 eV (Figure S9c), which is larger than the bulk values due to quantum confinement effects.^{19–21} As the particle size decreases to the nanoscale, the electron and hole carriers are more spatially confined, which enhances the Coulomb interaction between them. This stronger interaction increases the energy required to separate them.

The type of electronic transition in ferrite nanoparticles remains uncertain due to the combination of the quantum confinement effect and the complex nature of the spinel structure. Assuming indirect transitions, two distinct band gap energies are observed for all samples (Figure S9b). The pure CO nanoparticles show bandgap energies of 1.7 and 1.5 eV, corresponding to absorbance peaks at 250 and 660 nm. Similarly, pure CFO has bandgap energies of 2.0 eV and 2.4 eV, though its mixed valency complicates the determination of their origins. The bandgap energies for the CS of 3.3 eV and 2.0 eV align well with literature values.¹⁵

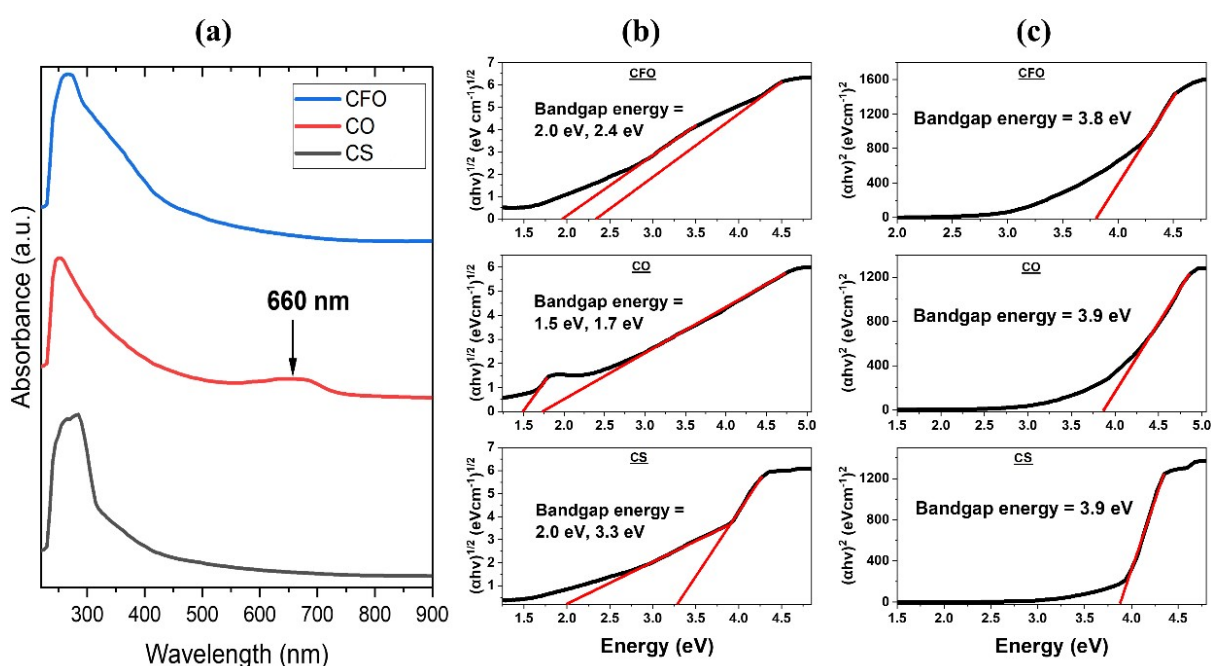


Figure S9. a) UV-Vis of all samples with the corresponding b) indirect and c) direct Tauc plots.

11. References

- 1 V. Crist, Iron (Fe), Z=26, & Iron Compounds, <https://xpsdatabase.net/iron-fe-z26-chemicals>, (accessed May 18, 2025).
- 2 H. Chen, Y. Fan, Z. Fan, H. Xu, D. Cui, C. Xue and W. Zhang, *Ceramics International*, 2021, **47**, 35057–35066.
- 3 K. Yang, H. Peng, Y. Wen and N. Li, *Applied Surface Science*, 2010, **256**, 3093–3097.
- 4 N. Shukla, C. Liu, P. M. Jones and D. Weller, *Journal of Magnetism and Magnetic Materials*, 2003, **266**, 178–184.

- 5 W. a. P. J. Premaratne, W. M. G. I. Priyadarshana, S. H. P. Gunawardena and A. A. P. D. Alwis, *Journal of Science of the University of Kelaniya*, DOI:10.4038/josuk.v8i0.7238.
- 6 I. O. P. D. Berti, M. V. Cagnoli, G. Pecchi, J. L. Alessandrini, S. J. Stewart, J. F. Bengoa and S. G. Marchetti, *Nanotechnology*, 2013, **24**, 175601.
- 7 Md. Amir, A. Baykal, H. Sözeri, H. Güngüneş and S. E. Shirsath, *Arabian Journal of Chemistry*, 2019, **12**, 4971–4981.
- 8 F. Wang, S. Javaid, W. Chen, A. Wang, M. A. Buntine and G. Jia, *Aust. J. Chem.*, 2021, **74**, 179.
- 9 A. K. Giri, K. Pellerin, W. Pongsaksawad, M. Sorescu and S. A. Majetich, *IEEE Transactions on Magnetics*, 2000, **36**, 3029–3031.
- 10 A. J. Cinthia, R. Rajeswarapalanichamy and K. Iyakutti, *Zeitschrift für Naturforschung A*, 2015, **70**, 797–804.
- 11 X. He, X. Song, W. Qiao, Z. Li, X. Zhang, S. Yan, W. Zhong and Y. Du, *J. Phys. Chem. C*, 2015, **119**, 9550–9559.
- 12 A. Almontasser and A. Parveen, *Sci Rep*, 2022, **12**, 7922.
- 13 I. Apostolova, A. Apostolov and J. Wesselinowa, *Applied Sciences*, 2023, **13**, 6411.
- 14 P. Makuła, M. Pacia and W. Macyk, *J. Phys. Chem. Lett.*, 2018, **9**, 6814–6817.
- 15 K. Shahzad, M. A. Abbasi, A. Jabeen, M. Zaman, U. Shehzad and M. H. Rafe, *Phys. Scr.*, 2024, **99**, 085942.
- 16 J. Klein, L. Kampermann, B. Mockenhaupt, M. Behrens, J. Strunk and G. Bacher, *Advanced Functional Materials*, 2023, **33**, 2304523.
- 17 B. Rivas-Murias and V. Salgueiriño, *Journal of Raman Spectroscopy*, 2017, **48**, 837–841.
- 18 A. V. Ravindra, B. C. Behera and P. Padhan, *J. nanosci. nanotech.*, 2014, **14**, 5591–5595.
- 19 S. Farhadi, M. Javanmard and G. Nadri, *Acta Chim Slov*, 2016, **63**, 335–343.
- 20 N. M. Refat, M. Y. Nassar and S. A. Sadeek, *RSC Advances*, 2022, **12**, 25081–25095.
- 21 A. V. Ravindra, M. Chandrika, Ch. Rajesh, P. Kollu, S. Ju and S. D. Ramarao, *Eur. Phys. J. Plus*, 2019, **134**, 296.